# Shape parameters of a floating bubble

Baburaj A. Puthanveettil, Akash Saha, Sangeeth Krishnan, Emil J. Hopfinger

▶ **To cite this version:**

Baburaj A. Puthanveettil, Akash Saha, Sangeeth Krishnan, Emil J. Hopfinger. Shape parameters of a floating bubble. Physics of Fluids, 2018, 30 (11), pp.112105. 10.1063/1.5052379 . hal-02058334

**HAL Id: hal-02058334**
**https://hal.science/hal-02058334v1**

Submitted on 15 Oct 2024

**HAL** is a multi-disciplinary open access archive for the deposit and dissemination of scientific research documents, whether they are published or not. The documents may come from teaching and research institutions in France or abroad, or from public or private research centers.

L'archive ouverte pluridisciplinaire **HAL**, est destinée au dépôt et à la diffusion de documents scientifiques de niveau recherche, publiés ou non, émanant des établissements d'enseignement et de recherche français ou étrangers, des laboratoires publics ou privés.

# Shape parameters of a floating bubble

Baburaj A. Puthenveettil,[1] Akash Saha,[2] Sangeeth Krishnan,[1,a)] and E. J. Hopfinger[3]
[1]*Department of Applied Mechanics, Indian Institute of Technology Madras, Chennai 600036, India*
[2]*Department of Mechanical Engineering, Jadavpur University, Jadavpur, Kolkata 700032, India*
[3]*LEGI-CNRS-UGA, BP 53, 38041 Grenoble Cedex 9, France*

(Received 17 August 2018; accepted 30 October 2018; published online 26 November 2018)

For a floating bubble, in the range of Bond numbers based on an equivalent spherical radius, $0 < Bo_e < 1$, we present analytical expressions for various shape parameters of the bubble as functions of $Bo_e$. Expressions are obtained for the radius of the rim $R_r$, the radius of the thin film cap $R_c$, the height of the top of the cap from the rim $h_{cap}$, the height of the rim above the free surface $h_r$, and the depth of the bubble cavity from the free surface $Z_c$. To obtain these expressions, we solve equations formulated in terms of these shape parameters for the meniscus outside the bubble, the force balance of the bubble, the pressure balance at the centre line of the bubble, and geometrical constraints, after neglecting the deformation of the bubble cavity for $Bo_e < 1$. The obtained expressions are shown to match well with our experimental measurements of the shape of the bubble. In addition to these expressions, we also present simpler approximations that can be used accurately as scaling laws for these shape parameters up to $Bo_e < 0.5$. *Published by AIP Publishing.* https://doi.org/10.1063/1.5052379

## I. INTRODUCTION

Many of the dynamic phenomena involving bubbles floating at liquid-gas interfaces are critically dependent on the static shape of these floating bubbles. These dynamic phenomena include collapse and ensuing jetting,[1–4] aerosol formation from the bubble cap,[5] coalescence of multiple bubbles,[6] the approach of the bubbles close to a solid surface,[7–9] and film draining at the free surface (FS) in foams.[10,11] Scaling laws of these phenomena have been limited due to the non-availability of the dependence of the parameters of the static shape of the bubble on gravity and surface tension. In this paper, by using equations of force balance and geometric constraints, formulated in terms of the shape parameters, we obtain expressions for these shape parameters of floating bubbles, which are shown to be valid till gravitational forces start to substantially deform the bubble cavity.

### A. Background

The shape of a static bubble floating at a liquid-gas interface is made up of the shape of its three interfaces, namely, the thin film cap at the top of the bubble, the meniscus of the liquid around the bubble that rises above the liquid surface, and the bubble cavity that is submerged within the liquid, as shown in Fig. 1(c). The thin film cap is spherical with a radius $R_c$, if the weight of the film is negligible and the cap has the same density gas on either of its sides; the equilibrium pressure balance then results in $p_i = p_o + 4\sigma/R_c$, where $p_i$ and $p_o$ are the internal and external gas pressures, respectively, and $\sigma$ is the liquid-gas interfacial tension. Neglecting the density of the gas, the shape of the meniscus of the liquid is determined by $\rho g(z - Z_c) = \sigma(1/R_1 + 1/R_2)$, where $R_1$ and $R_2$ are the principal radii of curvatures at the point with co-ordinates $(r, z)$ on the meniscus, with the origin at the bottom of the bubble cavity, $Z_c$ is the depth of the cavity bottom from the free surface, as shown in Fig. 1(e), $\rho$ is the density of the liquid, and $g$ is the acceleration due to gravity. The bubble cavity shape is decided by the pressure balance at any point $(r, z)$ on the cavity surface given by $\rho g(Z_c - z) = \sigma(1/R_1 + 1/R_2)$. Replacing the principal curvatures in terms of $r$ and $\phi$, the angle that the tangent to the surface at the point $(r, z)$ makes with the horizontal, a set of two differential equations in terms of $r$ and $\phi$ are obtained for the meniscus and the cavity surface. Even though no analytical solutions of these equations are available, they have been solved numerically using appropriate boundary conditions[5,12–17] to obtain the complete shape of a floating bubble and its associated meniscus.

However, in the study of dynamic phenomena associated with floating bubbles, to obtain scaling laws, it is not the complete shape of the bubbles that is needed but expressions for the important parameters that define the shape of such bubbles. For example, the velocity of jet that is ejected at the end of the collapse of a floating bubble, normalized by the capillary velocity, scales as the dimensionless depth of the cavity $Z_c^+ = Z_c/R_e$, where $R_e$ is the equivalent spherical radius of the bubble.[1,18] The amount of aerosols generated in this process is determined by the mass of the thin film cap $2\pi R_c h_{cap} t_c \rho$, where, as shown in Fig. 1(e), $h_{cap}$ is the height of the top of the thin film cap above the circle at which the three interfaces join, which we refer to as the rim [see Fig. 1(c)] and $t_c$ is the thickness of the thin film cap.[5] The force of attraction along the interface felt by a bubble floating close to another bubble is $\pi R\sigma\tilde{R}_r^2 \sin\phi_r$,[6] where $R$ is the radius of the bubble cavity, $\tilde{R}_r = R_r/R$ is the dimensionless radius of the rim $R_r$ [see Fig. 1(e)], and $\phi_r$ is the inclination angle with the horizontal of the tangent to the free surface at the rim. Hereinafter, all superscripts $\tilde{}$ denote normalization with $R$, the radius of the bubble cavity, while superscripts $^+$ indicate normalization with

[a)]Present address: ICTS-TIFR, Bengaluru, India.

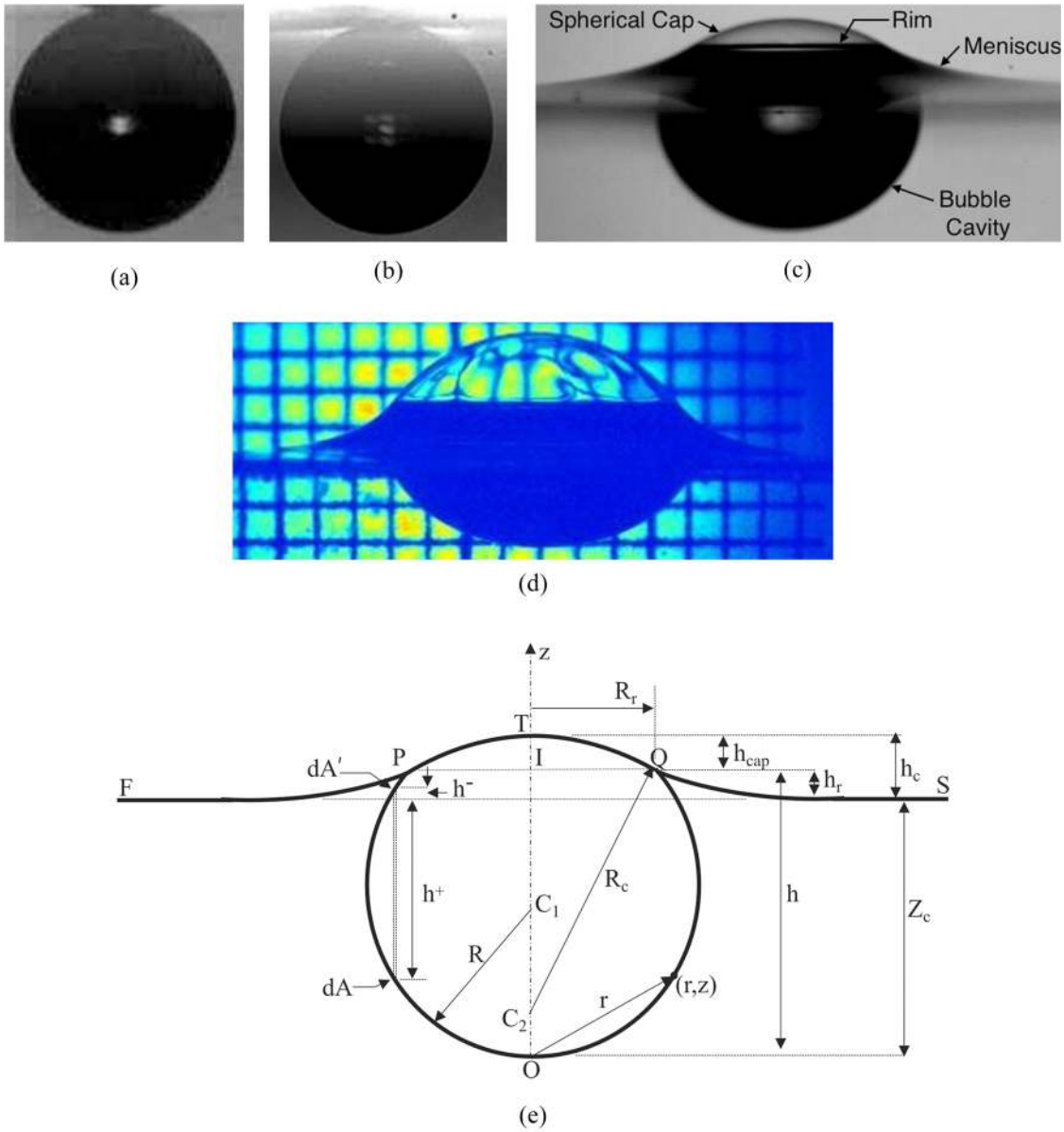


FIG. 1. [(a)–(d)] Side views of floating air bubbles at different Bond numbers. (a) $R_e = 0.175$ mm, $Bo_e = 0.004$; (b) $R_e = 0.47$ mm, $Bo_e = 0.03$; (c) $R_e = 1.99$ mm, $Bo_e = 0.5$; (d) $R_e = 3.61$ mm, $Bo_e = 2.46$; (e) schematic of a floating bubble with the present notation $h_c = h_{cap} + h_r$.

$R_e$, the equivalent spherical radius of the bubble. The approach of a bubble close to a horizontal solid surface is related to how fast the horizontal film, of area $\pi R_r^2$, between the bubble and the solid surface drains.[7,8] The thickness of the thin film during its draining at a free surface is related to the surface area of the thin film cap $2\pi R_c h_{cap}$.[10] The relations for all of these important dynamic phenomena associated with floating bubbles have shape parameters of the static bubbles floating at the interface, namely, $R_c$, $R_r$, $h_{cap}$, and $Z_c$, in them; closed form expressions for these would help in obtaining scaling laws for these dynamic phenomena.

### B. The *Bo* ≪ 1 limit

These shape parameters are functions of *Bo* since the shape of a floating bubble depends on its Bond number $Bo = \rho g R^2/\sigma$, as could be seen in Figs. 1(a)–1(d). Simple relations for these parameters in the limit of $Bo \ll 1$ have been obtained,[5,6,14,17,19] with the large *Bo* limit explored recently.[20] The two interfaces in the cap implies that $p_i - p_o = 4\sigma/R_c$. The pressure at the bottom of the bubble cavity in the liquid $p_b = p_o + \rho g Z_c$ due to the static pressure balance in the liquid. After neglecting the density of gas compared to that of the liquid, the pressure inside the bubble cavity at its bottom $p_i - p_b = 2\sigma/R$ due to a single interface at the bottom of the cavity. These equations can then be combined to obtain

$$Bo\tilde{Z}_c = \left(\frac{4}{\tilde{R}_c} - 2\right), \tag{1}$$

where $\tilde{Z}_c = Z_c/R$ is the dimensionless cavity depth and $\tilde{R}_c = R_c/R$ is the dimensionless cap radius. In the limit of $Bo \ll 1$, since the curvatures become quite large compared to the cavity depth for small bubbles, (1) becomes[19]

$$\tilde{R}_c = 2, \tag{2}$$

which also implies that $R_c \to 0$ when $Bo \to 0$. Since $R = R_e$ for small bubbles, $R_c^+ = 2$, where $R_c^+ = R_c/R_e$.

Similarly, in the limit of $Bo \ll 1$, considering that the vertical component of the surface tension force in the outer interface of the cap balances the upward buoyant force of the bubble, we obtain $4\pi R_e^3 \rho g/3 = \sigma \sin\phi_r 2\pi R_r$. Using $\sin\phi_r = R_r/R_c$, and (2), we obtain $R_r^+ = 2\sqrt{Bo_e/3}$, where $Bo_e$ is the Bond number based on $R_e$.[5,6,14] Again, since $R = R_e$ for small bubbles,

$$\tilde{R}_r = 2\sqrt{Bo/3}. \tag{3}$$

Since the inscribed angle at P by the arc TQ is $\phi_r/2$ [see Fig. 1(e)], the height of the thin film cap above the rim $h_{cap} = R_r \tan(\phi_r/2)$, which becomes equal to $R_r \sin(\phi_r/2)$ in the limit of $Bo \ll 1$. Using $\sin\phi_r = R_r/R_c$ and (3) in this equation, we obtain[14]

$$\tilde{h}_{cap} = \frac{1}{3}Bo, \tag{4}$$

the same expression in terms of $h_{cap}^+$ and $Bo_e$ being also valid in the small $Bo$ limit. Substituting (2) in (1), $\lim_{Bo\ll 1} Z_c = 0$, trivially so, since (2) has been obtained from (1) when $Z_c \to 0$. A more realistic expression for $Z_c$ has been obtained by Krishnan *et al.*[1] by assuming that the whole floating bubble remains spherical up to $Bo \approx 1$ to get

$$Z_c^+ = 2\sqrt{1 - \frac{2}{3}Bo_e}, \tag{5}$$

which however tends to a limit of 2 when $Bo \ll 1$; this limiting value of $Z_c \to 0$ as $R_e \to 0$ when $Bo \to 0$. A better approximation to $Z_c$ was also obtained by Krishnan *et al.*[1] by assuming the bubble to be an oblate spheroid. These however remain as geometric approximations with unclear physical basis and do not match quite well with the experimental variations.[1] The shape of floating bubbles very close to $Bo = 0$ was also obtained by perturbation methods.[15,21,22] In addition to being at very small $Bo$, the resulting expressions of shape parameters cannot be evaluated since they are in terms of other unknown shape parameters; furthermore, such expressions are available only for few of the shape parameters.

### C. Present work

From the discussion above, it is clear that even though the complete shapes of floating bubbles can be obtained numerically, no expressions for the important parameters that define the shape of such bubbles are available, except in the $Bo \ll 1$ limit. Shape equations of a point on the three interfaces of a floating bubble, in terms of $r$ and $\phi$, can only be solved numerically, failing to give explicit expressions for these shape parameters. These shape parameters critically decide many of the dynamic phenomena involving floating bubbles like collapse and jetting, coalescence, aerosolisation of the cap, and approach to a surface. The present work originated in our earlier work,[1] wherein we found that the dimensionless jet velocity from bubble collapse at a free surface scales as $Z_c/R_e$; however, no accurate closed form expressions for $Z_c$, or for other shape parameters, valid for $0 < Bo < 1$ were available. In this paper, we overcome this deficiency by obtaining expressions for the important shape parameters of a floating bubble for $0 < Bo < 1$. Using the force balances of the meniscus and the entire bubble, pressure balance at the vertical centre line, and geometric constraints, we first formulate equations explicitly in terms of the shape parameters of a floating bubble for $Bo \leq 1$. Solving these equations, we then obtain analytical expressions for the shape parameters of floating bubbles in terms of $Bo$ that are valid up to $Bo \leq 1$; these expressions are then verified by comparing with our measurements and the results from the literature. In addition, by using asymptotic expressions for some of these shape parameters in the relations between these parameters, we obtain simpler, but approximate, scaling laws for these shape parameters that are valid up to $Bo \leq 0.5$. These expressions for the shape parameters of floating bubbles can now be used to obtain scaling laws for many of the dynamic phenomena involving floating bubbles.

## II. EXPERIMENTS

The experiments to measure the shape parameters of floating bubbles were conducted in a transparent acrylic tank of $3.5 \times 5$ cm$^2$ cross-sectional area and in a glass tank of $5 \times 5$ cm$^2$ cross-sectional area. The tanks were fixed on a leveling board and were filled up to the brim to avoid meniscus effects. We used distilled water, glycerol-water mixtures of 48%, 55%, 68%, and 72% glycerin concentration (hereinafter referred to as GW48, GW55, GW68, GW72), ethanol, and 2-propanol; the properties of all these fluids[23] are given in Table I. The liquids were changed after each run to minimize surface contamination. Gas bubbles in the range of equivalent spherical radii 0.18 mm $< R_e <$ 4.1 mm were produced by pumping air into glass capillary tubes of different sizes using a syringe pump operated at a constant discharge rate. The flow rate in the capillaries was selected so that the bubble detachment was within the periodic bubbling regime.[24] Capillaries were carefully fixed in the same alignment through out the

TABLE I. Properties of the fluids and the range of equivalent radii and Bond numbers.

| Symbol | Fluid | $R_e$ (mm) | $Bo_e$ | $\sigma$ (kg s$^{-2}$) | $\rho$ (kg m$^{-3}$) |
|---|---|---|---|---|---|
| ◁ | Ethanol (20 °C) | 0.19–1.16 | 0.013–0.47 | 0.022 | 789 |
| + | 2-propanol (20 °C) | 1.46–2.41 | 0.9–2.4 | 0.018 | 781 |
| △ | Water (20 °C) | 0.18–4.08 | 0.004–2.27 | 0.072 | 1000 |
| ☆ | GW48 (30 °C) | 0.42–3.4 | 0.029–1.9 | 0.068 | 1115 |
| ☆ | GW48 (20 °C) | 0.81–1.96 | 0.1–0.62 | 0.068 | 1120 |
| □ | GW55 (20 °C) | 0.71–2.3 | 0.083–0.88 | 0.067 | 1140 |
| ▽ | GW68 (30 °C) | 0.48–2.3 | 0.041–0.89 | 0.066 | 1170 |
| ◇ | GW72 (30 °C) | 0.6–3.6 | 0.063–2.36 | 0.064 | 1181 |

experiments to avoid variations in bubble sizes.[25] The experiments were conducted in a temperature controlled laboratory after the temperature stabilized to the set values of 20 °C or 30 °C.

The bubbles rose to the free surface and stayed at the free surface for a short time after its initial oscillations had died down, before bursting. The elliptical shape of the rising bubbles[26] was photographed using high speed cameras (La Vision ProHS for fps ≤19 000 fps and Photron SA4 for fps ≤100 000) using high intensity light-emitting diode (LED) back lighting. The bubble volumes were calculated from these images, from which the equivalent spherical radii $R_e$ were calculated. The shape of the bubble at the free surface was also captured using the same cameras. The shape parameters were measured only from those images which were captured after the oscillations of the bubble died down and before they burst. There were no shape changes in the bubbles after they became static at the free surface and before they burst. This time of the stationary state of the bubble at the free surface was $t_s = 91$ ms for the smallest bubble in our experiments (water, $Bo_e = 4.2 \times 10^{-3}$), which increased to more than $t_s = 1$ s with increasing $Bo_e$. The time of acquisition of the images for these bubbles varied from $t_i = 10$ $\mu$s (1/100 000 fps) to 0.25 ms (1/4000 fps). Since $t_s/t_i \geq 4000$, shape changes occurred only after time durations greater than 4000 times the time of image acquisition; there were no shape changes during the image acquisition period.

The lowest resolution and the highest resolution of the images were 27 $\mu$m/pix and 3.4 $\mu$m/pix, respectively, while the smallest length measured was about 47.6 $\mu$m at a resolution of 6.8 $\mu$m/pix. The length scales were measured after calibrating the images with micrometer scales in both the air and liquid regions; for large bubbles, coarse grids were used as the background [see Fig. 1(d)]. Measurements were performed either in air or in the liquid region and not across the interface. An estimated error of ±2 pixels is expected in the length measurements, the corresponding error bars are shown in the following figures.

## III. THEORETICAL RELATIONS FOR SHAPE PARAMETERS

Consider a bubble in static equilibrium at the horizontal surface of a fluid, as shown in Fig. 1(e). We choose the coordinates $r$ and $z$ along the directions shown in Fig. 1(e). The bubble creates three interfaces. The thin film cap PTQ separating the bubble from the atmosphere is spherical and centered at $C_2$ with a radius of $R_c$. The bubble displaces the liquid close to itself upwards from the initially horizontal free surface FS to form a meniscus QS all around it. The third interface is the interface of the submerged part of the bubble or in other words the bubble cavity POQ.

### A. Assumptions

For any submerged spherical cavity of radius $R$, the difference in hydrostatic pressure over a depth $R$, which causes departure of the shape of the cavity from a spherical form, is $\rho gR$. The internal pressure due to the surface tension $\sigma$ is $2\sigma/R$. The bubble cavity will be nearly spherical when $2\sigma/R > \rho gR$, i.e., when the Bond number $Bo = \rho gR^2/\sigma = (R/l_c)^2 < 2$, where $l_c = \sqrt{\sigma/(\rho g)}$ is the capillary length. Since our analysis is limited to $Bo < 1$, we neglect the deviation of the shape of the bubble cavity from spherical for the present analysis. We hence assume that POQ, the bubble cavity submerged below the free surface and centered at $C_1$, to be spherical with a radius equal to $R$.

We also assume that the slope of the meniscus is small so that $(dz/dr)^2 \ll 1$ at all points of the meniscus for $Bo < 1$. The maximum value of $dz/dr$ of the meniscus occurs at $r = R_r$, which from geometry is

$$\left.\frac{dz}{dr}\right|_{r=R_r} = -\frac{R_r}{\sqrt{R_c^2 - R_r^2}}. \tag{6}$$

From our experimental measurements, at $Bo_e = 1$, $R_r/R_e \approx 0.85$ (see Sec. III F), while $R_c/R_e \approx 1.425$ (see Sec. III G); $(dz/dr)^2 \approx 0.55 < 1$. Thus the maximum value of $dz/dr$, at the maximum limit of the present analysis, i.e., at $Bo \leq 1$, does not quite satisfy the condition $(dz/dr)^2 \ll 1$. However, the average slope of the meniscus would indeed be less than one over its full length even for this maximum $Bo$. For lower values of $Bo$, less than one, even $\left.dz/dr\right|_{r=R_r} \ll 1$, the average slope being even lower.

### B. The meniscus surrounding the bubble

At any point $(r, z)$ on the meniscus surrounding the rim of the bubble, the height of the liquid above the free surface will be $z - Z_c$ and the principal radii of curvature are given by

$$\frac{1}{R_1} + \frac{1}{R_2} = \frac{d^2z/dr^2}{(1 + (dz/dr)^2)^{3/2}} + \frac{dz/dr}{r\sqrt{1 + (dz/dr)^2}}. \tag{7}$$

For $(dz/dr)^2 \ll 1$, (7) reduces to

$$\frac{1}{R_1} + \frac{1}{R_2} \approx \frac{d^2z}{dr^2} + \frac{1}{r}\frac{dz}{dr} = \frac{1}{r}\frac{d}{dr}\left(r\frac{dz}{dr}\right). \tag{8}$$

By equating the pressure drop in crossing the meniscus $\sigma(1/R_1 + 1/R_2)$ with the hydrostatic pressure at any point at a height of $z - Z_c$ above the level FS, we obtain

$$\frac{1}{r}\frac{d}{dr}\left(r\frac{dz}{dr}\right) = \frac{\rho g(z - Z_c)}{\sigma}. \tag{9}$$

In the dimensionless form, (9) becomes the modified Bessel equation of order zero,

$$\frac{1}{\tilde{r}}\frac{d}{d\tilde{r}}\left(\tilde{r}\frac{d\tilde{z}}{d\tilde{r}}\right) = Bo(\tilde{z} - \tilde{Z}_c), \tag{10}$$

where $\tilde{r} = r/R$, $\tilde{z} = z/R$, and $\tilde{Z}_c = Z_c/R$. The only solution of (10) which tends to $\tilde{Z}_c$ as $\tilde{r} \to \infty$ is

$$\tilde{z} = \tilde{Z}_c + CK_0\left(\tilde{r}\sqrt{Bo}\right), \tag{11}$$

where $C$ is a constant that needs to be determined from the boundary conditions and $K_0$ is the modified Bessel function of the second kind of order zero.

Now that the boundary condition at infinity is satisfied, we need to find $C$ that satisfies the boundary condition at the rim radius $\tilde{r} = \tilde{R}_r$, where $\tilde{R}_r = R_r/R$. From the geometry of

the cap shown in Fig. 1(e), the slope of the thin film cap PTQ at $\tilde{r} = \tilde{R}_r$ is $IQ/IC_2$, giving us

$$\frac{d\tilde{z}}{d\tilde{r}}\Big|_{\tilde{r}=\tilde{R}_r} = -\frac{\tilde{R}_r}{\sqrt{\tilde{R}_c^2 - \tilde{R}_r^2}}. \tag{12}$$

Since this slope has to be the same as the slope of the meniscus at $r = R_r$, taking the derivative of (11) with respect to $\tilde{r}$, and equating the result to (12), we obtain

$$C = \frac{\tilde{R}_r}{\sqrt{Bo\left(\tilde{R}_c^2 - \tilde{R}_r^2\right)}K_1(\tilde{R}_r\sqrt{Bo})}, \tag{13}$$

where $K_1 = -K_0{}'$, with $'$ representing the first derivative of $K_0$ with respect to its argument.

### C. Force balance of the entire bubble

The vertical force balance on the bubble between the net upward buoyancy force $B$ and the force of surface tension $\sigma 2\pi R_r$ acting downwards on the ring of radius $R_r$ at an angle $\phi_r$ gives

$$\sigma 2\pi R_r \sin\phi_r = B. \tag{14}$$

The net upward buoyancy force in (14)

$$B = \int_A p dA_z - \int_{A'} p dA'_z - p_a \pi R_r^2, \tag{15}$$

where $A$ is the surface area of the bubble cavity below FS, $A'$ is the surface area of the bubble cavity above FS and below PQ, and the subscript $z$ denotes the components of the elemental areas $dA$ and $dA'$ perpendicular to the $z$ axis [see Fig. 1(e)]. Since the pressure on the bubble surface at the level FS is atmospheric, the pressures on the points on the bubble surface at distances $h^+$ and $h^-$ below and above the free surface level [see Fig. 1(e)] are $p_a + \rho g h^+$ and $p_a - \rho g h^-$, respectively. Substituting these values of pressures in (15), we obtain

$$\begin{aligned} B = {} & p_a\left(\int_A dA_z - \int_{A'} dA'_z\right) \\ & + \rho g\left(\int_A h^+ dA_z + \int_{A'} h^- dA'_z\right) - p_a \pi R_r^2. \end{aligned} \tag{16}$$

Let us denote the volume of the bubble below the rim PQ to be $V$, the volume below the level FS to be $V'$, and that between PQ and FS excluding the cylindrical volume $\pi R_r^2 h_r$ to be $V''$,

$$V'' = V - V' - \pi R_r^2 h_r, \tag{17}$$

where $h_r$ is the height of the rim from the free surface level FS [see Fig. 1(e)]. Since $h^+ dA_z = dV'$, $h^- dA'_z = dV''$, and $\int_A dA_z - \int_{A'} dA'_z = \pi R_r^2$, by using (17), we obtain

$$B = \rho g\left(\int_{V'} dV' + \int_{V''} dV''\right) = \rho g(V - \pi R_r^2 h_r). \tag{18}$$

Equation (18) implies that due to the negative pressures on the surface of the bubble cavity between PQ and FS, the net buoyancy force is less than $\rho g V$, the weight of the liquid displaced by the bubble cavity.

The bubble cavity below PQ, assumed spherical, of depth $h$ and radius $R$, has a volume

$$V = \frac{\pi h^2}{3}(3R - h), \tag{19}$$

where $h = R + \sqrt{R^2 - R_r^2}$. The dimensionless depth

$$\tilde{h} = h/R = 1 + \sqrt{1 - \tilde{R}_r^2}, \tag{20}$$

using which

$$V = \frac{\pi R^3}{3}\left(\tilde{h}^2(3 - \tilde{h})\right). \tag{21}$$

Rewriting (21) in terms of $\tilde{R}_r$ using (20), we obtain

$$V = \frac{2\pi R^3}{3}\left(1 + \left(1 + \frac{\tilde{R}_r^2}{2}\right)\sqrt{1 - \tilde{R}_r^2}\right). \tag{22}$$

Substituting (22) in (18) and the resulting equation in (14), after simplifying, we obtain

$$B = \frac{2}{3}\pi R^3 \rho g\left(1 + \left(1 + \frac{\tilde{R}_r^2}{2}\right)\sqrt{1 - \tilde{R}_r^2} - \frac{3}{2}\tilde{R}_r^2 \tilde{h}_r\right), \tag{23}$$

where $\tilde{h}_r = h_r/R$. As can be seen from Fig. 1(e),

$$\tilde{h}_r = \tilde{z}\Big|_{\tilde{r}=\tilde{R}_r} - \tilde{Z}_c. \tag{24}$$

Equations (24) and (11) imply that

$$\tilde{h}_r = CK_0(\tilde{R}_r\sqrt{Bo}). \tag{25}$$

Substituting (25) in (23), replacing $B$ using (14), with $\sin\phi_r = R_r/R_c$, substituting the value of $C$ from (13), and rearranging give us

$$\tilde{R}_r^2 = \frac{\tilde{R}_c}{3}Bo\left(1 + \left(1 + \frac{\tilde{R}_r^2}{2}\right)\sqrt{1 - \tilde{R}_r^2} - \frac{3\tilde{R}_r^3\mu}{2\sqrt{Bo(\tilde{R}_c^2 - \tilde{R}_r^2)}}\right), \tag{26}$$

where

$$\mu = \frac{K_0(\tilde{R}_r\sqrt{Bo})}{K_1(\tilde{R}_r\sqrt{Bo})}. \tag{27}$$

As we show later by comparing with the numerical solutions of (26), neglecting the second and the third order terms in $\tilde{R}_r$ in (26) does not cause significant error in the estimate of $\tilde{R}_r$ up to $Bo \sim 1$. Hence, by dropping the second and third order terms in $\tilde{R}_r$ in (26), we obtain

$$\tilde{R}_r^2 = \frac{\tilde{R}_c}{3}Bo\left(1 + \sqrt{1 - \tilde{R}_r^2}\right). \tag{28}$$

In (28), since $\tilde{R}_c$ and $\tilde{R}_r$ are both unknown, we need two more equations to solve for both of them, which we now obtain from the pressure balance at the centerline of the bubble and from geometric constraints.

### D. Pressure balance at the centre line

Since the spherical cap at the top, of radius $R_c$, consists of two interfaces, the pressure excess inside the bubble is $4\sigma/R_c$. The pressure excess above the atmospheric pressure at the outer surface of the bubble at its lowest point O is $\rho g Z_c$ since this point is at a depth of $Z_c$ from the horizontal free surface. Therefore, the pressure excess inside the bubble at its lowest point is $\rho g Z_c + 2\sigma/R$. Since the density of the gas in the bubble is negligible compared to the density of the liquid outside, both these excess pressures have to be the same, implying

$$\frac{4\sigma}{R_c} = \frac{2\sigma}{R} + \rho g Z_c. \tag{29}$$

In the dimensionless form, (29) becomes

$$\frac{4}{\tilde{R}_c} = 2 + Bo\tilde{Z}_c, \tag{30}$$

the same equation as (1), which gives us another equation for $\tilde{R}_c$. Equations (28) and (30) still cannot be solved since there are three unknowns $\tilde{R}_r$, $\tilde{R}_c$, and $\tilde{Z}_c$. Hence, we need one more equation to obtain closed form expressions for $\tilde{R}_r$, $\tilde{R}_c$, and $\tilde{Z}_c$, which we now obtain from the geometrical relation for the depth of the bubble cavity.

### E. Geometric constraint

From the geometry of the bubble shown in Fig. 1(e), we obtain

$$Z_c = R + \sqrt{R^2 - R_r^2} - h_r, \tag{31}$$

which, in dimensionless form, is

$$\tilde{Z}_c = 1 + \sqrt{1 - \tilde{R}_r^2} - \tilde{h}_r. \tag{32}$$

Substituting $\tilde{h}_r$ from (25) and $C$ from (13) in (32), we obtain

$$\tilde{Z}_c = 1 + \sqrt{1 - \tilde{R}_r^2} - \frac{\tilde{R}_r\mu}{\sqrt{Bo\left(\tilde{R}_c^2 - \tilde{R}_r^2\right)}}. \tag{33}$$

We now have three Eqs. (28), (30), and (33) in three unknowns $\tilde{R}_r$, $\tilde{R}_c$, and $\tilde{Z}_c$, which can hence be solved to obtain expressions for these variables as functions of $Bo$.

### F. The dimensionless rim radius $\tilde{R}_r$

For $Bo < 1$, the terms in (32) have progressively smaller magnitudes with the last term of (32) being of order 0.1 since $h_r \ll R$, while the first two terms are of order one. As our results later show, neglecting $\tilde{h}_r$ in (32) for $Bo < 1$ does not result in significant error in the estimate of $\tilde{R}_r$. Hence, we drop the last term in (33) when we estimate $\tilde{R}_r$ and not anywhere else. Substituting $\tilde{Z}_c$ from (33), without the last term, in (30), and using the resulting expression for $\tilde{R}_c$ in (28), rearranging and simplifying, we obtain

$$\eta^2 Bo^2 - 12(Bo + 1)\eta + 48 = 0, \tag{34}$$

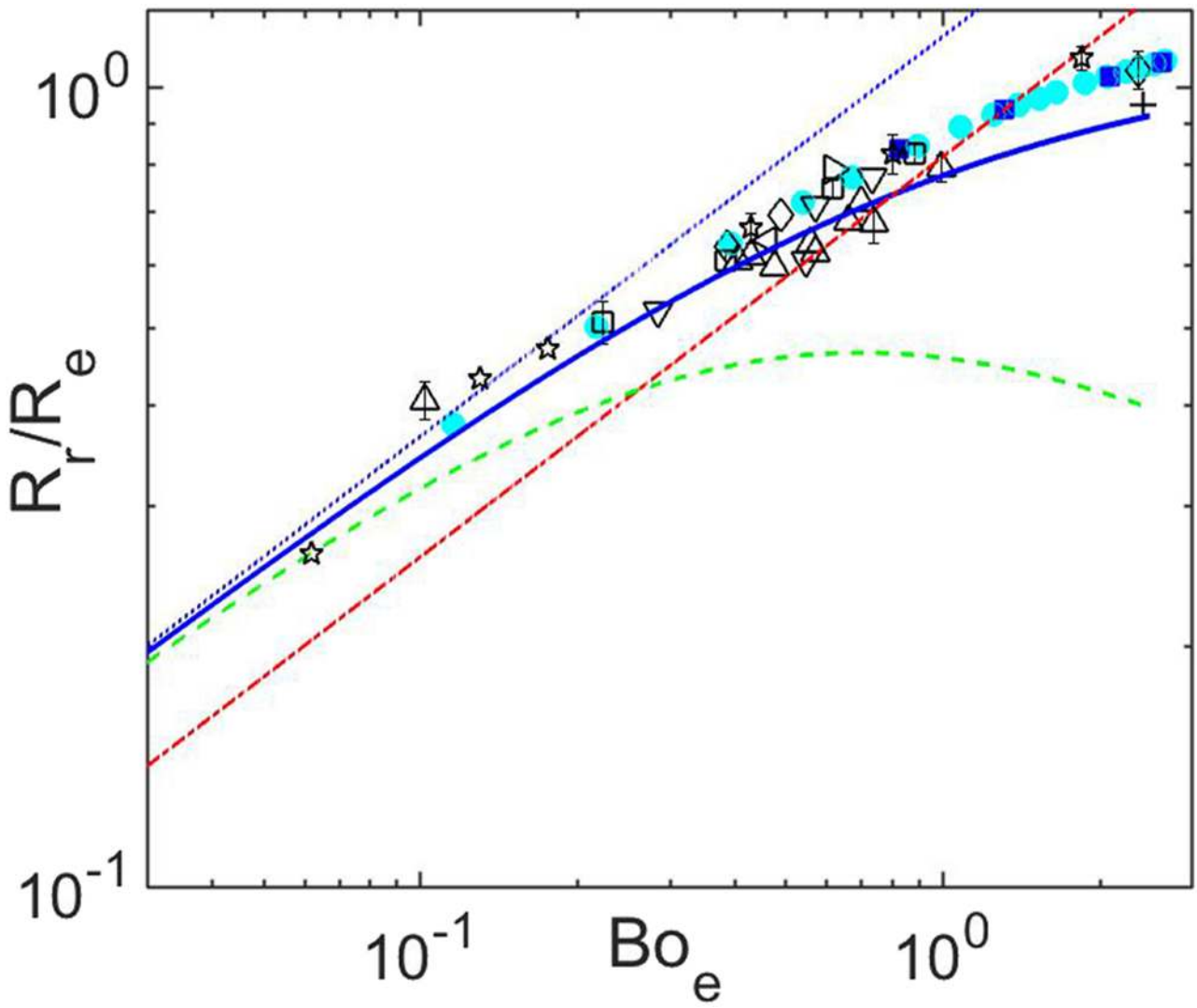


FIG. 2. Variation of the dimensionless rim radius $R_r^+$ with the Bond number. Black open triangles, water; black open stars, GW48; black open squares, GW55; black open inverted triangles, GW68; black open diamonds, GW72; black open left-pointing triangles, ethanol; black plus, 2-propanol; light blue filled circles, Princen;[14] blue filled squares, Medrow and Chao;[15] blue solid line, (36); red dotted-dashed line, $\sqrt{2Bo/3}$ (39); blue dotted line, $2\sqrt{Bo/3}$ (3); green dashed line, (40).

where

$$\eta = 4 - 3\tilde{R}_r^2. \tag{35}$$

Solving the quadratic equation (34) for $\eta$ and using the resulting expression in (35), we obtain $\tilde{R}_r^2$ as a series in $Bo$ in the form

$$\tilde{R}_r^2 = \frac{4}{3} - 2\left(\frac{1}{Bo} + \frac{1}{Bo^2}\right) + \sqrt{-\frac{4}{3Bo^2} + \frac{8}{Bo^3} + \frac{4}{Bo^4}}. \tag{36}$$

If we define $\beta = \sqrt{-4/(3Bo^2) + 8/Bo^3 + 4/Bo^4}$ and $\alpha = 2(1/Bo + 1/Bo^2)$, with

$$\Gamma = \alpha - \beta - 1/3, \tag{37}$$

(36) could be rewritten as

$$\tilde{R}_r = \sqrt{1 - \Gamma}. \tag{38}$$

Expression (36) has the appropriate limit of $\tilde{R}_r \to 0$ as $Bo \to 0$. The theory predicts that $\tilde{R}_r \to 2/\sqrt{3}$ for $Bo \to \infty$, implying a linear variation of $R_r$ with $R$. Even though this may not be a valid limit since the analysis is valid only up to $Bo \simeq 2$, the measurements do show an approximate constant $\tilde{R}_r$ at $Bo \approx 3$ (see Fig. 2).

Figure 2 shows the variation of $\tilde{R}_r$ from (36) along with our experimental measurements, the earlier numerical solutions,[14,15] the spherical approximation,[1,9,17,27]

$$\tilde{R}_r = \sqrt{2Bo/3}, \tag{39}$$

the power law approximation (3) using the low $Bo$ asymptote (2),[6] and the perturbation solution by Howell,[22]

$$R_r^+ = R_c^+\left(\frac{\sin 2\tilde{s}}{2} + Bo_e R_c^{+^2}\left(\frac{5\sin 2\tilde{s} - \sin 4\tilde{s}}{48} - \frac{\tilde{s}\cos 2\tilde{s}}{8}\right)\right), \tag{40}$$

where $\tilde{s} \sim \pi/2 - \sqrt{Bo_e}R_c^+/2\sqrt{3} + \pi Bo_e R_c^{+^2}/16$. Among coinciding numerical results,[13,15] only one[15] of them is included for comparison hereafter. To compare our theoretical results that are normalized with $R$, the bubble cavity radius, with our experimental results and the results from the literature, which are normalized with the equivalent spherical radius of the bubble $R_e$, we need to convert the former to the latter. Since $\tilde{R}_r \approx R_r^+$ for our theoretical expressions for $Bo_e < 1$ (see Appendix A), we plot $\tilde{R}_r$ of theory along with $R_r^+$ from our experiments and the literature in Fig. 2; the same is performed for other variables hereinafter.

Figure 2 makes it clear that, in general, there is no power law variation of $\tilde{R}_r$ valid over the whole range of $0 < Bo_e < 1$, as is also shown by (36). However, up to $Bo_e < 0.1$, the variation of $\tilde{R}_r$ with $Bo_e$ predicted by (36) shows a power law with an exponent of half, the same as that given by (3), (39), and (40); the same behavior is shown by our experimental measurements and all the earlier numerical solutions.[14,15] The experimental trend of $R_r^+$ with $Bo_e$ plateaus at larger $Bo_e$ (36) agrees well with this trend till $Bo_e \sim 1$, with the deviation of (36) with the experimental data being within the 2 pixel measurement error shown in the figure. The proposed expression (36) also approximates the numerical solutions[14,15] well for $Bo < 1$, even though it slightly underpredicts, with the underprediction being about 8% at $Bo \sim 1$. The perturbation solution (40) cannot be evaluated since the variation of $R_c^+$ with $Bo_e$ in (40) is not known. We however evaluate (40) using our expression of $\tilde{R}_c$, given later as (42), to show (40) as the green dashed line in Fig. 2; (40) deviates from the trend at around $Bo_e \sim 0.1$. For $0 < Bo_e < 1$, (36) is then a good approximation for $\tilde{R}_r$, which has the limit (3) for $Bo_e \to 0.1$, shown by the dotted line in Fig. 2. Equation (3) can then be used as a simple scaling law to predict $\tilde{R}_r$ up to $Bo_e < 0.1$, while (36) can be used so up to $Bo_e < 1$. The spherical approximation (39) underpredicts the rim radius values at low $Bo$ and overpredicts them at higher $Bo$. At larger $Bo_e$, any assumed power law approximation of $\tilde{R}_r$ with $Bo_e$ will have only a very small range of validity.

### G. The dimensionless cap radius $\tilde{R}_c$

Substituting (33) in (30), we obtain

$$\tilde{R}_c = \frac{4}{2 + Bo\left(1 + \sqrt{1 - \tilde{R}_r^2} - \tilde{R}_r\mu/\sqrt{Bo\left(\tilde{R}_c^2 - \tilde{R}_r^2\right)}\right)}, \tag{41}$$

which can be solved for $\tilde{R}_c$, as shown in Appendix B, to obtain

$$\tilde{R}_c = \frac{4 + \tilde{R}_r\mu\sqrt{Bo}}{2 + Bo\left(1 + \sqrt{1 - \tilde{R}_r^2}\right)}, \tag{42}$$

where $\tilde{R}_r$ is given by (36). Substituting (36) in (42), we obtain the expression for $\tilde{R}_c$ in terms of $Bo$ as

$$\tilde{R}_c = \frac{4 + \mu\xi\sqrt{Bo}}{2 + Bo\zeta}, \tag{43}$$

where

$$\xi = \sqrt{1 - \Gamma}, \tag{44}$$

$$\zeta = 1 + \sqrt{\Gamma}, \tag{45}$$

with $\Gamma$ given by (37) and $\mu$ given by (27).

Figure 3 shows the present analytical solution (43) along with the variation of $\tilde{R}_c$ measured from our experiments and the numerical solutions.[14,15] The present theory matches our experimental measurements well for $Bo_e < 1$. At around $Bo \sim 1$, the experimental measurements of $R_c$ deviates from the trend of the experimental data till then, as well as from (43). One possible reason could be the increasing importance of drainage in the thin film at larger $Bo$,[5] which could change the shape of the thin film cap from the assumed spherical one in the theory.

The numerical computations[14,15] however deviate strongly from the present experimental data and (43) from $Bo_e$ as low as 0.02. Deviations of the actual shape of the bubble from the assumed spherical shape of the cap and the cavity, as well as the assumed low slope of the meniscus, in the theory will not even be noticeable up to $Bo < 0.1$; the deviations are expected to be significant only when $Bo > 1$. Hence the cause for these surprising deviations of $R_c$ in theory from that in simulations is unlikely to be due to the assumptions in theory since the deviations start at very low $Bo$, and at these low $Bo$, the assumptions in the theory are supported well by experiments. Similarly, the higher order terms that are dropped in the theory affect mostly the derivation of $R_r$ [see (28) and (34) in Secs. III C and III F]. The expression for $R_r$ (36) obtained in this way matches fairly

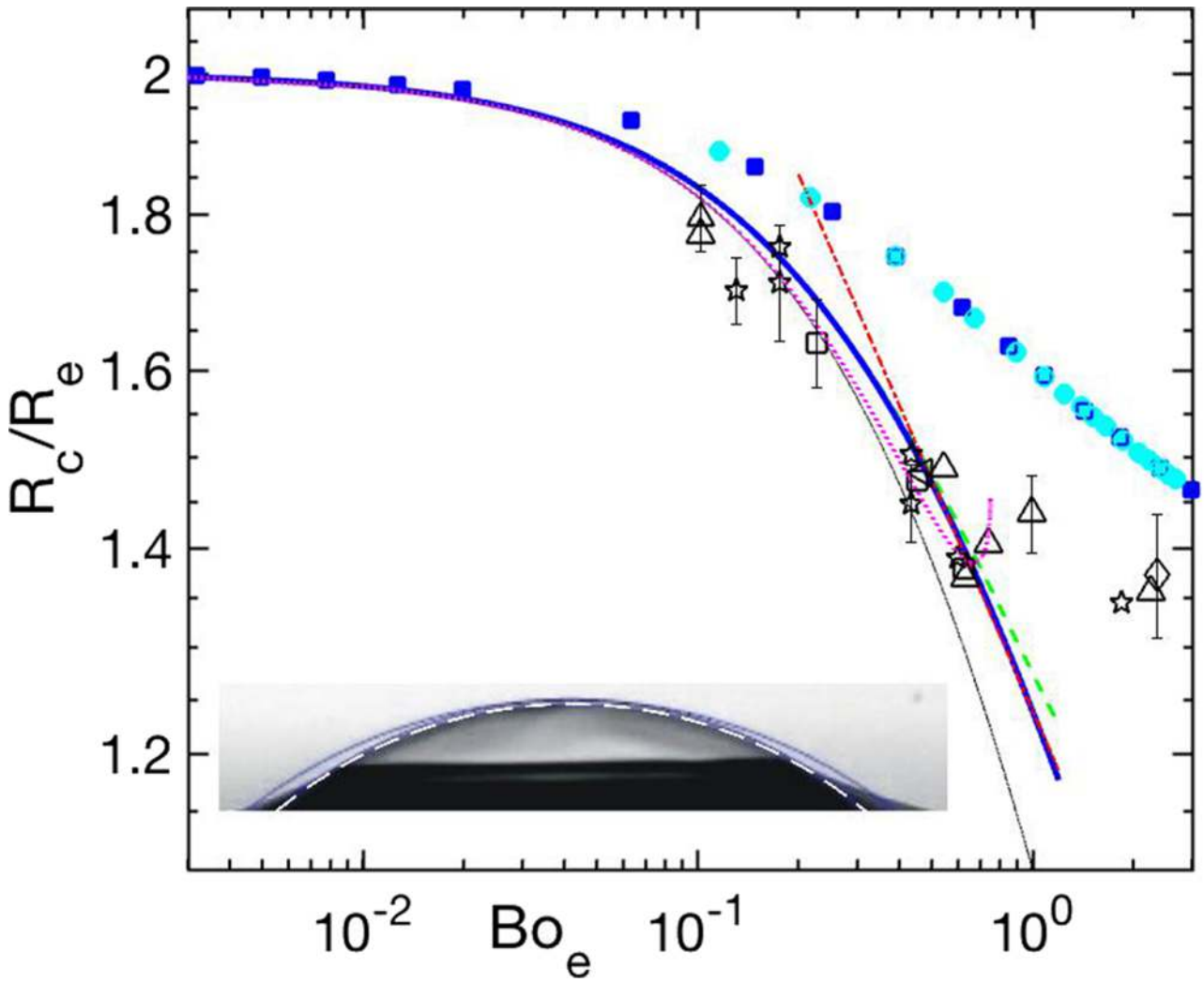


FIG. 3. Variation of the dimensionless cap radius with the Bond number. Experimental measurements in black open triangles, water; black open stars, GW48; black open squares, GW55; black open diamonds, GW72; black open left-pointing triangles, ethanol; light blue filled circles, Princen;[14] blue filled squares, Medrow and Chao;[15] blue solid line, (43), the analytical root of (B5) using $\gamma$ from (B10); green dashed line, the numerical root of (B1); black solid line, the analytical root of (B5) using $\gamma$ from (B11). Larger numerical and analytical roots alone are shown. Pink dotted line, the simpler scaling law, (47); red dotted-dashed line, the $Bo \to 1$ limit (46). The inset shows the spherical cap for a bubble of $R_e = 1.64$ mm in GW48 at $Bo_e = 0.4326$ along with the circle corresponding to $\tilde{R}_c = 1.75$ predicted by numerical simulations (blue circle) and $\tilde{R}_c = 1.5$ measured in experiments (white dashed circle).

well with the experiments. Hence, even though the approximate expression of $R_r$ (36) is used in the final expression for $R_c$ (41), since $R_r$ matches fairly well with experiments, this cannot be the reason for the deviation of the theoretical results of $R_c$ from the simulations.

Furthermore, and most importantly, the numerical solution also deviates from the experimental measurements, far beyond the range of error in the experiments. To verify this, we show in the inset of Fig. 3 the blue circle of radius $\tilde{R}_c = 1.75$ predicted by the numerical solutions for $Bo_e = 0.4326$, along with the white dashed circle from which $\tilde{R}_c = 1.5$ was measured for an image in GW48 at the same $Bo_e$. The circle from the latter coincides with the spherical cap, while that corresponding to the predictions of numerical solutions is much larger and unrealistic. We hence expect that the deviation of (43) from the numerical simulations is not due to the approximations made in the theoretical analysis but due to something missing in the numerical simulations. We are unable to comment on the exact reason for this discrepancy in simulations since we do not know the details of the simulations.

Equation (43) shows that there is no simple power law expression for $\tilde{R}_c$ as a function of $Bo$ for $0 < Bo < 1$. As per (42), $\tilde{R}_c \to 2$ when $Bo \ll 1$, in agreement with (2) obtained based on the physical argument[19] for the limiting case of small bubbles. Figure 3 shows that $\tilde{R}_c = 2$ is however valid only for very small bubbles up to $Bo_e < 0.01$. In the limit $Bo_e \to 1$,

$$R_c^+ = 1.24 Bo_e^{-1/4} \tag{46}$$

fits the variation of $R_c^+$ with $Bo_e$ for $0.3 < Bo_e < 1$, as shown in Fig. 3. As per (43), $\tilde{R}_c \sim \mu\sqrt{Bo}/Bo$ for $Bo \to 1$; (46) is an approximate limiting form of (43) since $\mu$ scales as $Bo^{1/4}$ for $Bo \to 1$.

A non-power law scaling, much simpler than (43), could also be obtained by substituting (32) without the last term in (30), replacing $\tilde{R}_r$ with (3), and rearranging to obtain

$$\tilde{R}_c = \frac{4}{2 + Bo(1 + \sqrt{1 - 4Bo/3})}. \tag{47}$$

Figure 3 shows that (47) is quite accurate in the range $0 < Bo_e < 0.6$ and can hence be used as a simple scaling relation for $\tilde{R}_c$ for $Bo_e < 0.6$. By proposing (47), we extend (2), the earlier available relationship for $R_c$, from its validity of $Bo < 0.01$ to $Bo < 0.6$, while (43) extends the same to $Bo < 1$.

### H. Height of the rim and the cap

The rim PQ in Fig. 1(e) is at a height $h_r$ above the horizontal free surface FS. The corresponding dimensionless height $\tilde{h}_r$ can be obtained by evaluating (11) at $\tilde{r} = \tilde{R}_r$ to obtain

$$\tilde{z}\Big|_{\tilde{r}=\tilde{R}_r} - \tilde{Z}_c = \tilde{h}_r = CK_0(\tilde{R}_r\sqrt{Bo}). \tag{48}$$

Substituting the value of $C$ from (13), we obtain

$$\tilde{h}_r = \frac{\tilde{R}_r \mu}{\sqrt{Bo\left(\tilde{R}_c^2 - \tilde{R}_r^2\right)}}. \tag{49}$$

Substituting (38) and (43) for $\tilde{R}_r$ and $\tilde{R}_c$ in (49), we obtain $\tilde{h}_r$ in terms of $Bo$ as

$$\tilde{h}_r = \frac{\mu\xi\Delta}{\sqrt{Bo(\Lambda - \xi^2(\Delta^2 + 4\Delta_1^2))}}, \tag{50}$$

where

$$\Delta = 2 + Bo\zeta, \tag{51}$$

$$\Delta_1 = 1 + Bo\zeta, \tag{52}$$

$$\Lambda = 16 + 8\mu\xi\sqrt{Bo} + \xi^2\left(4 + Bo(\mu^2 + 4\zeta) + Bo^2\zeta^2\right), \tag{53}$$

with $\xi$ given by (44) and $\zeta$ given by (45).

A further approximation of (50), which results in a much simpler relation for $\tilde{h}_r$, can be obtained by replacing $\tilde{R}_r$ and $\tilde{R}_c$ in (49) with (3) and (2), respectively, and then using the approximation[28] for

$$\mu\left(\tilde{R}_r\sqrt{Bo}\right) = \left(1 + \frac{1}{\tilde{R}_r\sqrt{Bo}}\right)^{-1/2} \tag{54}$$

to obtain

$$\tilde{h}_r = \sqrt{\frac{2Bo}{\left(2Bo + \sqrt{3}\right)(3 - Bo)}}; \tag{55}$$

for $Bo \ll 1$, (55) reduces to

$$\tilde{h}_r = \sqrt{\frac{2Bo}{3^{3/2}}}. \tag{56}$$

From Fig. 1(e), the dimensionless height of the bubble cap above the rim is

$$\tilde{h}_{cap} = h_{cap}/R = \tilde{R}_c - \sqrt{\tilde{R}_c^2 - \tilde{R}_r^2}, \tag{57}$$

which when written in terms of $Bo$ using (38) and (43) become

$$\tilde{h}_{cap} = \frac{4 + \mu\xi\sqrt{Bo} - \sqrt{\Lambda - \xi^2(\Delta^2 + 4\Delta_1^2)}}{\Delta}. \tag{58}$$

A simpler approximation is obtained by replacing $\tilde{R}_r$ and $\tilde{R}_c$ in (57) with (3) and (2), respectively, to obtain

$$\tilde{h}_{cap} = 2(1 - \sqrt{1 - Bo/3}). \tag{59}$$

Alternatively, since $\tilde{h}_{cap} = \tilde{R}_r \tan(\phi_r/2)$, with $\tan(\phi_r/2) = \sin\phi_r/(1 + \cos\phi_r)$, replacing $\sin\phi_r = R_r/R_c$ and $\cos\phi_r = \sqrt{R_c^2 - R_r^2}/R_c$, we obtain $\tilde{h}_{cap} = \tilde{R}_r^2/\left(\tilde{R}_c + \sqrt{\tilde{R}_c^2 - \tilde{R}_r^2}\right)$, in which, by replacing $\tilde{R}_r$ with (3) and $\tilde{R}_c$ with (2), we obtain

$$\tilde{h}_{cap} = \frac{2Bo}{3(1 + \sqrt{1 - Bo/3})}, \tag{60}$$

which coincides with (59). When $Bo \ll 1$, (60) becomes (4) which then tends to zero when $Bo \to 0$, similar to the behavior of (59).

The dimensionless height of the top of the bubble above the free surface is then

$$\tilde{h}_c = h_c/R = \tilde{h}_r + \tilde{h}_{cap}, \tag{61}$$

with $\tilde{h}_r$ and $\tilde{h}_{cap}$ given by (50) and (58), where $h_c = h_{cap} + h_r$. The sum of (55) with (59) or (60) gives a simpler approximation for $\tilde{h}_c$.

Figure 4 shows the experimental variation of $\tilde{h}_c$ with $Bo_e$, along with the expression (61), where $\tilde{h}_r$ and $\tilde{h}_{cap}$ are given by (50) and (58). Some of the multiple measurements at the same $Bo_e$ are shown, the range of spread being shown by the error bars. Considering that the spread of the experimental data is not small, possibly due to the errors involved in measuring the small length $h_c$ at small $Bo_e$, a reasonably good match between the theory and experiments is observed. The figure also shows that the complex expression (61), where $\tilde{h}_r$ is given by (50) and $\tilde{h}_{cap}$ is given by (58), could be well approximated by a simple power law,

$$\tilde{h}_c = 0.78Bo_e^{3/5} \tag{62}$$

for $0 < Bo_e < 1$. The simplified expressions given by the sum of (55) and (59) or by the sum of (55) and (60) coincide on each other. As shown in Fig. 4, both follow the experimental results and (61) but are offset upwards by a small amount. This offset is an outcome of using (2), valid only for $Bo < 0.01$, to obtain (55). A better approximation could be obtained by using (47) instead of (2), at the expense of simplicity of the expression. Multiplying the sum of (55) and (59) by a pre-factor of 0.8, to account for the approximations in using (2), will also give a good match of the resulting expression with (61).

The top inset in Fig. 4 shows the experimental variation of $\tilde{h}_{cap}$, along with the variation predicted by (58) and the numerical solution.[14] An excellent match between the numerical results[14] and (58) is observed up to $Bo_e < 1$. The experimental results also follow the prediction of (58) with reasonable accuracy, given the spread of data shown by the error bars. The variation of $\tilde{h}_{cap}$ predicted by (4) is shown as a dashed-dotted line in the top inset. Even though the slope of (4) is higher than that shown by the numerical results[14] and (58), (4) is a close approximation to (58) and the numerical results.[14] It is surprising that (59) and (60), which coincide and are shown by the dashed line in the top inset, actually deviate more than (4) from (58) and the numerical results.[14] Considering the fairly close approximation that (4) makes to (58), the simplicity of equation (4) makes it a more convenient choice for use in scaling laws than (58).

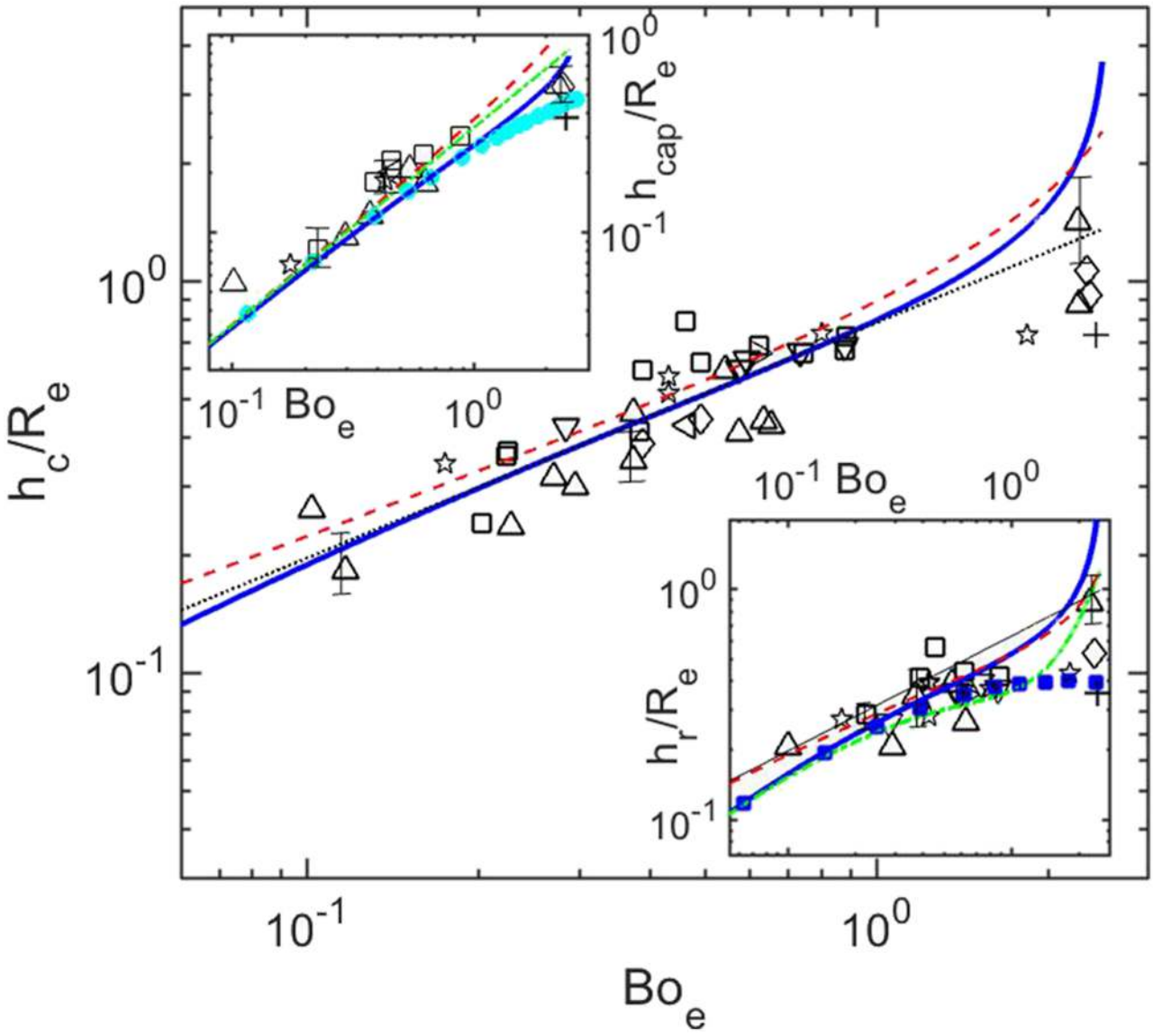


FIG. 4. Variation of the dimensionless height of the top of the bubble above the free surface with the Bond number. Black open triangles, Water; black open stars, GW48 black open squares, GW55; black open inverted triangles, GW68; black open diamonds, GW72; black open left-pointing triangles, ethanol; black plus, 2-propanol; blue solid line, (61) with $\tilde{h}_r$ given by (50) and $\tilde{h}_{cap}$ given by (58); black dotted line, $0.78Bo^{3/5}$ (62); red dashed line, sum of (55) and (60). The top inset shows the variation of the dimensionless height of the bubble cap above the rim with the Bond number. In the top inset, blue solid line, (58); green dotted-dashed line, (4); red dashed line, (60); light blue filled circles, Princen.[14] The bottom inset shows the variation of the dimensionless height of the rim above the free surface with the Bond number. In the bottom inset, thick blue solid line, (50); red dashed line, (55); thin black solid line, the small *Bo* limit (56); dotted-dashed green line, Kralchevsky *et al.*[21] (63); blue filled square, Medrow and Chao.[15]

The variation of the dimensionless height of the rim $\tilde{h}_r$ with $Bo_e$ in experiments is shown in the bottom inset in Fig. 4, along with (50), and the numerical results.[15] The numerical results[15] match (50) quite well up to $Bo_e \sim 0.6$. Considering the spread of the experimental data, shown by error bars, the experiments also follow (50) reasonably well. The only other available relation for $h_r$, obtained by Kralchevsky *et al.*[21] using perturbation expansion for small *Bo*, is

$$\frac{\tilde{h}_r}{\tilde{R}_r} = \chi_0 + \frac{\tilde{R}_r^2 Bo}{2}\left((\sin\psi_c + \chi_0\cos\psi_c)(1 + \chi_0\cot\psi_c - \frac{\cot\psi_c}{2}) - \frac{\chi_0}{2} + \frac{\sin^3\psi_c}{8}\right), \tag{63}$$

where $\psi_c = \sin^{-1}(\tilde{R}_r/\tilde{R}_c)$ and $\chi_0 = \sin\psi_c \ln(4/\gamma_e \tilde{R}_r\sqrt{Bo}(1 + \cos\psi_c))$, with $\gamma_e = 1.78$. However, the variation predicted by (63) could not be estimated since no closed form expressions for $\tilde{R}_r$ and $\tilde{R}_c$ were given by Kralchevsky *et al.*[21] We hence use our expressions for $\tilde{R}_r$ (36) and $\tilde{R}_c$ (42) in (63) to plot (63) in the bottom inset in Fig. 4 as the dashed-dotted line. Since (63) is valid only for small *Bo*, (63) deviates from (50) at $Bo_e \approx 0.2$; (50) approximates the experimental trends better up to $Bo_e \sim 1$. The simpler, approximate expression for $\tilde{h}_r$ (55) is shown in the bottom inset in Fig. 4 as the dashed line. Even though (55) is a fairly good approximation to (50), use of (2), which is valid only up to $Bo < 0.01$, to obtain (55) seems to result in a slight over prediction by (55). The small *Bo* limit (56), shown as the thin solid line in the bottom inset in Fig. 4,

when used with a pre-factor of 0.5, instead of the pre-factor of $\sqrt{2/3^{3/2}}$, would match (50) fairly well so as to be used as a simple scaling law.

### I. The dimensionless cavity depth $\tilde{Z}_c$

Now that we have expressions for $\tilde{R}_r$ and $\tilde{R}_c$ in terms of the Bond number in (38) and (43), we can substitute these in (33) to obtain $\tilde{Z}_c$ in terms of $Bo$ as

$$\tilde{Z}_c = \zeta - \frac{\mu\xi}{\Lambda}\left(\zeta + \frac{2}{Bo}\right), \tag{64}$$

where $\zeta, \xi$, and $\Lambda$ are given by (45), (44), and (53), respectively. As shown in Fig. 5, the variation of $\tilde{Z}_c$ with $Bo$ predicted by (64) matches the experimental variation well for $0 < Bo_e < 2$. Clearly, there is no single power law for $\tilde{Z}_c$ valid for $0 < Bo_e < 1$; any power law approximation of (64) will only be valid for a very short range of $Bo_e$. When $Bo_e \ll 1$, (64) tends to the correct limit of 2, similar to the spherical and the oblate spheroidal approximations[1] shown in Fig. 5. These approximations however start to deviate from the experimental variation for $Bo_e > 0.01$, again coming close to the experimental trends at $Bo_e \sim 1$; on the contrary, (64) follows the experimental trends well through out the range of $0 < Bo_e < 2$.

We can also find a simpler expression than (64), which is however a larger approximation than (64), by using (3) and (55) in (32), to obtain

$$\tilde{Z}_c = 1 + \sqrt{1 - \frac{4}{3}Bo} - \sqrt{\frac{2Bo}{(2Bo + \sqrt{3})(3 - Bo)}}. \tag{65}$$

Figure 5 shows that (65), which has real values only up to $Bo < 3/4$, is a fairly good approximation for $\tilde{Z}_c$ up to $Bo_e < 0.5$. Using the $Bo \ll 1$ limit of $\tilde{h}_r$ (56), instead of the last term in (65), we obtain

$$\tilde{Z}_c = 1 + \sqrt{1 - \frac{4}{3}Bo} - \sqrt{\frac{2Bo}{3^{3/2}}}, \tag{66}$$

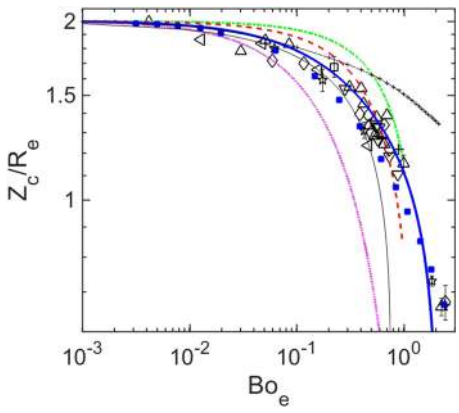


FIG. 5. Variation of the dimensionless cavity depth with the Bond number. Black open triangles, Water; black open stars, GW48; black open squares, GW55; black open inverted triangles GW68; black open diamonds, GW72; black open left-pointing triangles, ethanol; black plus, 2-propanol; blue filled squares, Medrow and Chao;[15] thick blue solid line, (64); thin black solid line, (65); pink dotted line, (67); green dotted-dashed line, spherical approximation (5); red dashed line, oblate spheroidal approximation;[1] black dashed plus, Howell.[22]

which almost coincides with (65). A better approximation than these two simple expressions could be obtained by using (47) in (49) and using the resultant expression for $\tilde{h}_r$ in (32), which will however result in a more complex expression than (65) and (66).

The expression for $\tilde{Z}_c$ from Kralchevsky *et al.*,[21] in terms of our notation, is

$$\tilde{Z}_c = 1 + \sqrt{1 - \tilde{R}_r^2} - \tilde{h}_r \pm Bo\, z_1, \tag{67}$$

where

$$z_1(\phi_c) = \frac{1}{3}\sin^2\phi_c + \frac{2}{3}\ln\sin\frac{\phi_c}{2} - \frac{1}{2}(1 + \cos\phi_c) \tag{68}$$

with $\phi_c = \sin^{-1}\tilde{R}_r$. The first three terms in (67) are exactly the same as in (32), since they are an outcome of the geometry, even though the expression for $\tilde{h}_r$ (63)[21] to be used in (67) is different from (49). The fourth term accounts for the deformation of the bubble cavity, which is neglected in the present analysis. However, expression (67) could not be estimated analytically since closed form expressions for $\tilde{R}_r$ and $\tilde{R}_c$ were not given by Kralchevsky *et al.*[21] Using the present expressions for $\tilde{R}_r$ and $\tilde{R}_c$, given by (36) and (42), we can evaluate $\tilde{Z}_c$ from (67), a plot of which is shown in Fig. 5. As expected, including deformation of the bubble cavity results in a lower value of $Z_c$ than the present estimates. The present experimental results shown in Fig. 5, with which (64) matches better, however show that the deformation of the bubble cavity is not significant for $Bo < 1$. Expression for $\tilde{Z}_c$ given by Howell,[22]

$$\tilde{Z}_c \sim \frac{\tilde{R}_c^3 Bo_e}{24}\left(-3\log(Bo_e\tilde{R}_c^2) - 2.08 - \frac{24}{Bo_e\tilde{R}_c^2}\right), \tag{69}$$

evaluated using our expression for $\tilde{R}_c$ (43) is shown in Fig. 5. Expression (69) follows the trend till $Bo_e < 0.1$, while (64) is a good approximation to the experimental $\tilde{Z}_c$ up to $Bo_e \sim 2$.

## IV. DISCUSSION AND CONCLUSIONS

The primary results of the paper are the new analytical expressions obtained for the shape parameters of a floating bubble, which match our experimental data well for the range $0 < Bo_e < 1$, where $Bo_e$ is the Bond number based on the equivalent spherical radius $R_e$. These shape parameters, namely, the rim radius $R_r$, cap radius $R_c$, cap heights $h_{cap}$ and $h_c$, rim height $h_r$, and depth of the bubble cavity $Z_c$, appear in scaling relations of dynamic phenomena associated with floating bubbles. Even though numerical solutions for the complete shape of these bubbles are available, no expressions for the various parameters describing their shape, as functions of $Bo_e$, are available for $0 < Bo_e < 1$, the usually encountered range of $Bo_e$; the present study fills this gap.

We find that the rim radius, known to scale as $R_r \sim R^2/l_c$ (3),[6] where $l_c = \sqrt{\sigma/\rho g}$ is the capillary length and $R$ is the bubble cavity radius, does so only up to $Bo_e < 0.1$, with $R_r$ becoming approximately linearly dependent on $R$ for $Bo_e \sim 1$. Our new proposed expression for the dimensionless rim radius,

$$\tilde{R}_r^2 = \frac{4}{3} - 2\left(\frac{1}{Bo} + \frac{1}{Bo^2}\right) + \sqrt{-\frac{4}{3Bo^2} + \frac{8}{Bo^3} + \frac{4}{Bo^4}},$$

(38) in the form of a series in $Bo$ valid for $Bo < 1$, where $Bo$ is the Bond number based on $R$, captures this initial $R^2$ dependence and the later linear trend with increasing $Bo_e$. The radius of the spherical thin film cap $R_c = 2R$, as was proposed earlier,[19] we show, is valid only for $Bo_e < 0.01$. We now extend this result to show that for $0.5 < Bo_e < 1$, $R_c \sim \sqrt{R_e l_c}$ (46), with

$$R_c = \frac{4R}{\left(2 + Bo(1 + \sqrt{1 - 4Bo/3})\right)},$$

(47) in the intermediate range of $0 < Bo_e < 0.5$; the complete solution for $R_c$ proposed in (43) for $0 < Bo_e < 1$ captures all these three trends.

The $Bo \ll 1$ asymptote for the height of the thin film cap above the rim, $h_{cap} \sim R^3/l_c^2$ (4),[14] is now formally obtained and is shown to be surprisingly close up to $Bo_e < 0.5$ to the complete solution (58), which is valid for $0 < Bo_e < 1$. The two alternative expressions for $h_{cap}$, (59) and

$$h_{cap} = \frac{2BoR}{3(1 + \sqrt{1 - Bo/3})}$$

(60) obtained for the intermediate range of $Bo$, which are simpler than (58), however seem to offer no advantage compared to the simple scaling law (4). We now obtain the scaling of the height of the rim above the free surface as $h_r \sim R^2/l_c$ (56) as a $Bo \ll 1$ asymptote of the scaling for the intermediate range of $Bo$

$$h_r = \sqrt{\frac{2BoR^2}{\left(2Bo + \sqrt{3}\right)(3 - Bo)}}$$

(55), which itself is an approximation of the complete solution that we obtain as (50). Unlike understood earlier,[1,17] $h_{cap}$ and $h_r$ do not scale in the same way, neither do they have the same magnitudes. Once the relations for $h_{cap}$ and $h_r$ are known, either complete or approximate, we obtain the expression for the height of the thin film cap above the free surface $h_c$ as the sum of $h_{cap}$ and $h_r$, which scales as $h_c \sim (R^7/l_c^4)^{1/3}$ (62).

The depth of the bottom of the bubble cavity $Z_c$, which decides the velocity of the jet coming out of the collapse of a floating bubble, was earlier estimated assuming the bubble to be spherical (5) or to be an oblate spheroid,[1] which however did not follow the experimental measurements closely. Our measurements show that there is no power law approximation possible for $Z_c$, except for the trivial case of $Z_c \sim 2R$ for $Bo_e < 0.01$, with $Z_c$ decreasing to $0.7R$ at $Bo_e \approx 1$. We now propose a relation (64) that matches this non-trivial experimental variation of $Z_c$ quite closely in the range $0 < Bo_e < 1$. Furthermore, we find a simple non-power law scaling,

$$Z_c = R\left(1 + \sqrt{1 - \frac{4}{3}Bo} - \sqrt{\frac{2Bo}{3^{3/2}}}\right)$$

(66), which is accurate up to $Bo_e < 0.5$.

Figures 2–5 show a consistent, but non-trivial, change in the shape of the bubble with an increase in $Bo_e$. Up to about $Bo_e = 0.1$, an increase in the radius of the bubble results in an increase in the rim radius proportional to $R^2$, with the cap radius and the cavity depth being proportional to the increase in $R$, while the cap and rim heights continue to increase as $R^2$ and $R^3$ in the whole range of $Bo_e < 1$. So the bubble expansion is the predominant process up to $Bo_e = 0.1$. With an increase in $Bo$ beyond 0.1, the predominant change in the bubble shape becomes that of a less than proportional increase in $R_c$ and $Z_c$, while the earlier rapid increase in the rim radius with $R$ slows down to a slower value; at the same time, the cap height continues to increase with the earlier trend. These behaviors mean that the upward displacement of the bubble starts to dominate for $Bo_e > 0.1$.

The expressions presented in this paper were obtained by solving the force balance of the meniscus and the entire bubble, pressure balance at the centre line, and geometrical constraints, assuming that the bubble cavity below the free surface remains spherical. Flattening of the bottom bubble cavity is hence neglected in the present analysis; this effect however seems to become important only at $Bo_e$ larger than one. Including an equation for the shape of the bottom bubble cavity, as against the spherical geometry assumed in the present analysis, results in unsolvable expressions. However, for larger $Bo_e$, these effects will have to be included to obtain accurate expressions for the shape parameters.

## ACKNOWLEDGMENTS

We gratefully acknowledge the partial financial support by DST, Govt. of India, under Grant Nos. SR/FST/ETII-017/2003 and SR/S3/MERC/028/2009, for this study.

## APPENDIX A: CONVERSION OF NORMALIZATION WITH $R$ TO NORMALIZATION WITH $R_e$ FOR THE PRESENT THEORY

The total bubble volume for the present assumed shape of the bubble

$$V_b = V_{cap} + V, \tag{A1}$$

where

$$V_b = \frac{4}{3}\pi R_e^3, \tag{A2}$$

$$V_{cap} = \frac{\pi}{3}h_{cap}^2(3R_c - h_{cap}), \tag{A3}$$

and

$$V = \frac{\pi}{3}(Z_c + h_r)^2(3R - Z_c - h_r) \tag{A4}$$

is the volume of the spherical cap below PQ, as defined in (21). Substituting (A2), (A3), and (A4) in (A1), we obtain the expression for $\tilde{R}_e = R_e/R$ as

$$\tilde{R}_e^3 = \frac{1}{4}\left(3\tilde{R}_c\tilde{h}_{cap}^2 - \tilde{h}_{cap}^3 + (\tilde{Z}_c + \tilde{h}_r)^2(3 - \tilde{Z}_c - \tilde{h}_r\right). \tag{A5}$$

The variation of $\tilde{R}_e$ with $Bo$, calculated using expressions (43), (58), (50), and (64) in (A5), is shown in Fig. 6; $\tilde{R}_e \approx 1$ for $Bo < 1$ for the present assumed theoretical configuration of the bubble. Since $\tilde{R}_r = R_r/R$ and $R_r^+ = R_r/R_e$,

$$R_r^+ = \tilde{R}_r/\tilde{R}_e, \tag{A6}$$

and similarly

$$Bo_e = Bo\tilde{R}_e^2, \tag{A7}$$

where $Bo_e = \rho g R_e^2/\sigma$. However since $\tilde{R}_e \approx 1$ from Fig. 6 for $Bo < 1$, we use $\tilde{R}_r = R_r^+$ and similarly for all other

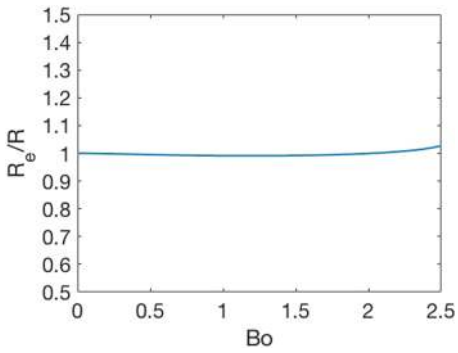


FIG. 6. Variation of the dimensionless equivalent spherical radii with the Bond number based on the bubble cavity radius for the present theory.

length variables for the present theoretical results; similarly, $Bo_e = Bo$ for the present theoretical results.

## APPENDIX B: SOLUTION OF (41) FOR $\tilde{R}_c$

Equation (41) can be simplified into the form of a fourth order polynomial

$$a_4\tilde{R}_c^4 + a_3\tilde{R}_c^3 + a_2\tilde{R}_c^2 + a_1\tilde{R}_c + a_0 = 0, \tag{B1}$$

where

$$\begin{aligned} a_4 &= A_1^2,\ a_3 = -2A_1A_2, \\ a_2 &= A_2^2 - \tilde{R}_r^2A_1^2 - \frac{\tilde{R}_r^2\mu^2}{Bo}, \\ a_1 &= 2A_1A_2\tilde{R}_r^2 \text{ and } a_0 = -\tilde{R}_r^2A_2^2. \end{aligned} \tag{B2}$$

Here,

$$A_1 = 1 + \sqrt{1-\tilde{R}_r^2} + \frac{2}{Bo} \quad \text{and} \quad A_2 = \frac{4}{Bo}, \tag{B3}$$

with $\tilde{R}_r$ being given by (36).

Equation (B1) may be written as

$$(\tilde{R}_c - \kappa)(\tilde{R}_c + \kappa)(\tilde{R}_c^2 + \delta\tilde{R}_c + \gamma) = 0, \tag{B4}$$

where $\kappa$ and -$\kappa$ are solutions which are less than 1 or negative and hence are not physically realistic solutions of (B1) since the dimensionless thin film cap radius $\tilde{R}_c$ cannot assume these values. The solution of (B1) is hence given by the two remaining roots of (B4), which are the roots of the quadratic equation

$$\tilde{R}_c^2 + \delta\tilde{R}_c + \gamma = 0. \tag{B5}$$

The coefficients $\delta$ and $\gamma$ of equation (B5) can now be found as follows. Expanding (B4) and writing it in the form of (B1) and by comparing the terms with (B1), we obtain

$$\frac{a_3}{a_4} = \delta,\ \frac{a_2}{a_4} = \gamma - \kappa^2,\ \frac{a_1}{a_4} = -\kappa^2\delta, \text{ and } \frac{a_0}{a_4} = -\gamma\kappa^2. \tag{B6}$$

It is also obvious from (B6a) and (B6c) that

$$-\frac{a_1}{a_3} = \kappa^2, \tag{B7}$$

which again is equal to $\tilde{R}_r^2$ from (B2b) and (B2d), so that

$$\kappa = \pm\tilde{R}_r. \tag{B8}$$

Using (B6a) and substituting for $a_3$ and $a_4$ from (B2b) and (B2a), we obtain by using (B3a) and (B3b)

$$\delta = \frac{-8}{2 + Bo\left(1 + \sqrt{1-\tilde{R}_r^2}\right)}. \tag{B9}$$

Substituting $a_2$ and $a_4$ from (B2c) and (B2a) in (B6b), using $A_1$ and $A_2$ from (B3a) and (B3b), and using (B9), we obtain

$$\gamma = \frac{16 - \tilde{R}_r^2\mu^2Bo}{\left(2 + Bo\left(1 + \sqrt{1-\tilde{R}_r^2}\right)\right)^2}. \tag{B10}$$

Similarly, substituting $a_0$ and $a_4$ from (B2e) and (B2a) in (B6d) and using (B8), we obtain

$$\gamma = \frac{16}{\left(2 + Bo\left(1 + \sqrt{1-\tilde{R}_r^2}\right)\right)^2}. \tag{B11}$$

Both (B10) and (B11) are possible expressions for $\gamma$. As shown in Fig. 3, the bigger root of (B5), obtained with $\gamma$ given by (B10), is a close approximation of the biggest numerical root of (B1), as well as the experimental data. Since the solution of (B5) using (B10) matches well with the numerical solution of (B1), and the experimental measurements, we choose (B10) as the expression for $\gamma$. Now, by solving (B5) using (B9) and (B10), we obtain the expression for the dimensionless cap radius as (42).

[1]S. Krishnan, E. J. Hopfinger, and B. A. Puthenveettil, "On the scaling of jetting from bubble collapse at a liquid surface," J. Fluid Mech. **822**, 791–812 (2017).
[2]E. Ghabache, A. Antkowiak, C. Josserand, and T. Séon, "On the physics of fizziness: How bubble bursting controls droplets ejection," Phys. Fluids **26**, 121701 (2014).
[3]P. L. L. Walls, L. Henaux, and J. C. Bird, "Jet drops from bursting bubbles: How gravity and viscosity couple to inhibit droplet production," Phys. Rev. E **92**, 021002 (2015).
[4]A. M. Gañán-Calvo, "Revision of bubble bursting: Universal scaling laws of top jet drop size and speed," Phys. Rev. Lett. **119**, 204502 (2017).
[5]H. Lhuissier and E. Villermaux, "Bursting bubble aerosols," J. Fluid Mech. **696**, 5–44 (2012).
[6]M. M. Nicolson, "The interaction between floating particles," Math. Proc. Cambridge Philos. Soc. **45**, 288–295 (1949).
[7]B. V. Derjaguin and M. M. Kussakov, "Experimental investigations on solvation of surfaces with application to the development of a mathematical theory of the stability of lyophobic colloids," Bull. Acad. Sci. URSS Ser. Chim. **5**, 1119 (1937).
[8]B. V. Derjaguin and M. M. Kussakov, "An experimental investigation of polymolecular solvate (adsorbed) films as applied to the development of a mathematical theory of the stability of colloids," Prog. Surf. Sci. **40**, 26–45 (1992).
[9]R. S. Allan, G. E. Charles, and S. G. Mason, "The approach of gas bubbles to a gas/liquid interface," J. Colloid Sci. **16**, 150–165 (1961).
[10]H. Kočárková, F. Rouyer, and F. Pigeonneau, "Film drainage of viscous liquid on top of bare bubble: Influence of the Bond number," Phys. Fluids **25**, 022105 (2013).
[11]C. Nguyen, H. Gonnermann, Y. Chen, C. Huber, A. Maiorano, A. Gouldstone, and J. Dufek, "Film drainage and the lifetime of bubbles," Geochem., Geophys., Geosyst. **14**, 3616–3631, https://doi.org/10.1002/ggge.20198 (2013).
[12]F. Bashforth and J. C. Adams, *An Attempt to Test the Theories of Capillary Action* (University Press, 1883).
[13]Y. Toba, "Drop production by bursting of air bubbles on the sea surface (II) theoretical study on the shape of floating bubbles," J. Oceanogr. Soc. Jpn. **15**, 121–130 (1959).
[14]H. Princen, "Shape of a fluid drop at a liquid-liquid interface," J. Colloid Sci. **18**, 178–195 (1963).
[15]R. A. Medrow and B. T. Chao, "Floating bubble configurations," Phys. Fluids **14**, 459–465 (1971).

[16]S. Hartland and R. W. Hartley, *Axisymmetric Fluid-Liquid Interfaces: Tables Giving the Shape of Sessile and Pendant Drops and External Menisci, with Examples of Their Use* (Elsevier Science Ltd., 1976).
[17]J. M. Boulton-Stone and J. R. Blake, "Gas bubbles bursting at a free surface," J. Fluid Mech. **254**, 437–466 (1993).
[18]K. Sangeeth, B. A. Puthenveettil, and E. Hopfinger, "Jet formation from bubble collapse at a free surface," in *Proceedings of 23rd International Congress of Theoretical and Applied Mechanics, Beijing*, edited by Y. Bai, J. Wang, and D. Fang (Elsevier, 2012), p. 171.
[19]D. C. Chappelear, "Models of a liquid drop approaching an interface," J. Colloid Sci. **16**, 186–190 (1961).
[20]C. Cohen, B. D. Texier, E. Reyssat, J. H. Snoeijer, D. Quéré, and C. Clanet, "On the shape of giant soap bubbles," Proc. Natl. Acad. Sci. U. S. A. **114**, 2515 (2017).
[21]P. A. Kralchevsky, I. B. Ivanov, and A. D. Nikolov, "Film and line tension effects on the attachment of particles to an interface: II. Shapes of the bubble (drop) and the external meniscus," J. Colloid Interface Sci. **112**, 108–121 (1986).
[22]P. D. Howell, "The draining of a two-dimensional bubble," J. Eng. Math. **35**, 251–272 (1999).
[23]*CRC Handbook of Chemistry and Physics*, 80th ed., edited by D. R. Lide (CRC Press, 2001).
[24]H. N. Oguz and A. Prosperetti, "Dynamics of bubble growth and detachment from a needle," J. Fluid Mech. **257**, 111–145 (1993).
[25]P. Doshi, I. Cohen, W. W. Zhang, M. Siegel, P. Howell, O. A. Basaran, and S. R. Nagel, "Persistence of memory in drop breakup: The breakdown of universality," Science **302**, 1185 (2003).
[26]D. Sharaf, A. Premlata, M. K. Tripathi, B. Karri, and K. C. Sahu, "Shapes and paths of an air bubble rising in quiescent liquids," Phys. Fluids **29**, 122104 (2017).
[27]T. Gillespie and E. K. Rideal, "The coalescence of drops at an oil-water interface," Trans. Faraday Soc. **52**, 173–183 (1956).
[28]E. A. Boucher and T. G. J. Jones, "Capillary phenomena. Part 11. Approximate treatment of the shape and properties of fluid interfaces of infinite extent meeting solids in a gravitational field," J. Chem. Soc., Faraday Trans. 1 **76**, 1419–1432 (1980).